RESEARCH PAPER

# Enhanced removal of chromate from aqueous solution by sequential adsorption–reduction on mesoporous iron–iron oxide nanocomposites

**Jae-Hwan Kim · Ji-Hun Kim · Varima Bokare · Eun-Ju Kim · Yoon-Young Chang · Yoon-Seok Chang**

**Abstract** The adsorption behavior of mesoporous iron nanocomposites was investigated with respect to chromate [Cr(VI)] removal from aqueous solutions to consider its application for purifying chromate-contaminated wastewaters. These nanocomposites were prepared by borohydride reduction in aqueous solutions containing varying concentrations of acetone as co-solvent. Using batch methods, enhanced adsorption of Cr(VI) on the nanocomposite surface was achieved at neutral pH conditions, which subsequently resulted in Cr(VI) reduction to Cr(III). The Langmuir model was found to excellently describe the adsorption process, offering a maximum adsorptive capacity of 34.1 mg/g for composites prepared with 50 % acetone concentration. The Cr(VI) removal efficiency of these iron nanocomposites is strongly dependent on the acetone concentration, as evident from their (1) increased surface area (141.1 m$^2$/g) compared to conventional iron nanoparticles (33.2 m$^2$/g), and (2) highly porous and acicular structure, which efficiently traps Cr(VI) through adsorption. X-ray photoelectron spectroscopy analysis of Cr(III) on the nanocomposite surface confirmed that Cr(VI) removal from solution was achieved by sequential adsorption–reduction.

## Introduction

Hexavalent chromium [Cr(VI)] is a highly priority heavy metal pollutant in nature and found extensively in wastewaters from leather tanning, electroplating, and metal processing industries (sometimes with concentration as high as 50,000 mg/L) (Kowalski 1994). In the environment, Cr(VI) species may be in the form of dichromate ($Cr_2O_7^{2-}$), hydrochromate ($Cr_2O_7^{2-}$), or chromate ($Cr_2O_7^{2-}$) in aqueous solution, depending on the pH (Park and Jang 2002). Due to repulsive electrostatic repulsions, Cr(VI) anionic species are poorly adsorbed by negatively charged soil particles in the environment, and hence, they are transferred easily in aqueous environments. Cr(VI) also causes health problems such as liver damage, pulmonary congestions, vomiting, and severe diarrhea (Lv et al. 2011; Shi et al. 2011). Due to the severe toxicity of Cr(VI), the EU Directive, WHO, and US EPA have set the maximum contaminant concentration of Cr(VI) in domestic water supplies as 0.05 mg/L. Such toxicity has warranted the need for

J.-H. Kim · J.-H. Kim · V. Bokare · E.-J. Kim · Y.-S. Chang (✉)
School of Environmental Science and Engineering, Pohang University of Science and Technology (POSTECH), Pohang 790-784, South Korea
e-mail: yschang@postech.ac.kr

Y.-Y. Chang
Department of Environmental Engineering, Kwangwoon University, Seoul 139-701, South Korea

the efficient and complete removal of Cr(VI) form industrial wastes.

Several treatment technologies have been implemented for the removal of Cr(VI) including precipitation, membrane filtration, ion exchange, and adsorption by activated carbon and biological adsorbents (Eisazadeh 2007; Gupta and Babu 2009; Zhu et al. 2011). However, besides adsorption by activated carbon, these methods have proven to be expensive, time consuming, rather inefficient, not very feasible for small scale industries and have resulted in the production of undesirable sludges (Pillay et al. 2009). To circumvent such problems, the most favorable route of Cr(VI) removal from water is by reduction to trivalent chromium [Cr(III)], which has low aqueous solubility and toxicity (Chang 2005). Further, more importantly, the positively charged Cr(III) species in aqueous solution (either in the form of $Cr^{3+}$, $Cr(OH)^{2+}$, or $[Cr(OH)_2]^{2+}$), can be easily adsorbed on the negatively charged soil particles, effectively inhibiting their mobility in the aqueous environment. Cr(VI) reduction has been demonstrated with $Fe^{2+}$ (Fendorf and Li 1996; Sedlak and Chan 1997; Pettine et al. 1998), magnetite ($Fe_3O_4$) (Kendelewicz et al. 2000), green rust (Bond and Fendorf 2003; Legrand et al. 2004), ferrous sulfate–sodium dithionite (Ludwig et al. 2007), granular zero-valent iron (ZVI) (Alowitz and Scherer 2002; Chen et al. 2007; Jeen et al. 2008; Flury et al. 2009) and nanoscale ZVI (Xu and Zhao 2007; Li et al. 2008). Although, the use of heterogeneous reductants provides high surface area for adsorption and precipitation, they are only efficient at lower pH (Chen et al. 2007) and hence, subsequent pH re-adjustment to near-neutral values is required to precipitate the Cr(III) ions. Under actual field condition, it is not feasible to change the pH of the polluted plumes, which is a major constraint for limited application of various catalysts as efficient agents for Cr(VI) remediation.

With this background, continuous research efforts are geared towards the development of new catalysts, which can absorb and reduce Cr(VI) over a wide pH range (especially at near-neutral pH). Zero-valent iron nanoparticles (nZVI) are now well established as effective and efficient reductants of a variety of chlorinated compounds such as tetrachloroethene (PCE), trichloroethene (TCE), and polychlorinated dibenzo-p-dioxin (PCDD) (Liu et al. 2007; Kim et al. 2008; Taghavy et al. 2010). However, the application of nZVI for on-site remediation faces several constraints, with the major challenge being nZVI aggregation. The agglomeration of nZVI particles is caused by self-assembly of nanoparticles due to magnetic interactions, Van der Waals attractions and electrostatic double layer repulsion (Jiang et al. 2011). Thus, improving the stability and dispersibility of the synthesized nZVI particles constitutes one of the important criteria for efficient remediation application.

The general method of synthesizing nZVI under laboratory conditions uses sodium borohydride-induced reduction of ferric ($Fe^{3+}$) salts (Wang and Zhang 1997). However, nZVI particles synthesized using these methods are essentially aggregates of individual nanoparticles (Carpenter 2001). Using capping agents like polymers (Schrick et al. 2004; Saleh et al. 2005; Bonder et al. 2007) or surfactants (Kanel and Choi 2007), surface modification of nZVI hinders particle aggregation and enhances dispersibility in solution (Saleh et al. 2008). The use of co-solvents during the synthesis of nZVI is also an efficient method to stabilize these nanoparticles (Wang et al. 2006, 2009). The presence of co-solvent reduces the nucleation and growth of individual nanoparticles, and provides control over shape, size, and structural phase of the nanoparticles (Margeat et al. 2005). Carbonyl solvents such as acetone, ethanol, and butane (those having C=O bonds), which can be selectively reduced by sodium borohydride, are considered useful additives to achieve porous, acicular iron/iron oxide core shell structures with lower boron content (Periasamy and Thirumalaikumar 2000).

The aim of this study was to synthesize iron–iron oxide core–shell nanocomposites, which exhibited dual properties of Cr(VI) adsorption (by iron oxide shell with large surface area) and reduction (by zero-valent Fe core) to non-toxic Cr(III). Using a simple co-solvent like acetone at optimum aqueous concentration, nanocomposite catalysts were easily prepared with controlled morphology and surface area. These nanocatalysts exhibited rapid Cr(VI) adsorption and subsequent reduction Cr(III). Compared to traditional iron nanoparticles, these nanocomposites exhibited higher dispersibility and stability. The dispersivity in aqueous phase as well as the size and the reactivity of these composites could be easily controlled by simply altering the acetone–water volume ratio during synthesis. More importantly, complete Cr(VI) removal

was achieved at near-neutral pH. A Langmuir isotherm was used to determine the chromium uptake and maximum adsorption capacity. XPS studies were undertaken to establish the Cr(VI) reduction products on the surface of the composites. 50 % acetone was determined as optimum concentration (v/v) for the synthesis of nanocomposites (with the highest surface area of 141.1 $m^2/g$) showing superior activity towards chromate reduction.

## Experimental

### Synthesis of iron nanocomposites

Iron nanocomposites were synthesized from 0.15 M $FeCl_3 \cdot 6H_2O$ (Kanto, Japan) in mixtures of water and acetone (acetone concentration was 0 (native nZVI), 5, 10, 25, and 50 % by volume (Merck, UK) and corresponding nanocomposites are designated as 0A, 5A, 10A, 25A and 50A, respectively. Prior to use, $FeCl_3$ solutions were deoxygenated by sparging with argon gas for 2 h and then reduction of $Fe^{3+}$ was accomplished by adding 0.24 M $NaBH_4$ (Sigma Aldrich). The reduction procedure was done under a flow of argon to prevent surface passivation of the particles during synthesis. The precipitate was centrifuged and washed with deoxygenated/deionized water and methanol (three times each). The precipitate was dried in a vacuum chamber overnight, and stored in anaerobic chamber. Nanocomposites at an optimum concentration of 50 % v/v were also synthesized using ethanol and methanol (Merck, UK) as co-solvents. To evaluate the Cr(VI) adsorption capacity of pure iron oxides, test experiments were performed using lepidocrocite [($\gamma$-FeOOH), Bayferrox 943] and magnetite [$Fe_3O_4$] (Sigma-Aldrich)].

### Characterization

The structure and composition of the nanocomposites was characterized by transmission electron microscopy (TEM, JEOL 4000FX operated at 400 kV), scanning electron microscopy equipped with energy-dispersive X-ray microanalysis (SEM-EDX, JEOL JSM-7401F operated at 5 kV), X-ray photoelectron spectroscopy (XPS, ESCALAB 220iXL with Mg K$\alpha$ X-ray source), X-ray powder diffraction (XRD,

Rigaku Dmax III with Cu K$\alpha$ radiation), light scattering for particle size distribution (Photal, Otsuka Electronics), $N_2$ gas adsorption–desorption (Micromeritics ASAP 2000) and magnetometry for saturation magnetization ($B_s$) (TOEI KOGYO VSM-5 magnetometer and B–H analyzer). $Fe^0$ ( %) content ($\chi_{Fe(0)}$) of the synthetic iron was estimated from the amount of $H_2$ evolution in concentrated HCl by gas chromatography (GC-TCD) according to the procedure of Liu et al. (2005).

### Kinetics of Cr(VI) removal

$K_2CrO_4$ (Sigma Aldrich) was used as source of Cr(VI). 1,000 mg/L chromate stock solution was prepared and its pH adjusted to 6.0 by 0.1 N HCl. Nanocomposites of different concentrations (15–1,500 mg/L) were suspended in deoxygenated/deionized water using 50 mL serum bottles. The Cr(VI) stock was added into these solutions with the final Cr(VI) concentration fixed at 20 mg/L. Serum bottles were placed on a roll mixer (15 rpm) and kept in a dark room at 20 °C during reaction. Periodically, reactors were sacrificed for analysis by filtering sample through a 0.45 μm filter (Millipore). No pH buffers were used during the course of the experiment. The final pH at the end of the experiment was between 6.0 and 8.2 for all samples. The solution pH increased due to the formation of hydroxide ions during corrosive oxidation of metallic iron. Total Cr in the solution was determined using inductively coupled plasma-optical emission spectroscopy (ICP-OES, Varian) and Cr(VI) concentration was measured by UV–Vis spectrophotometry at 540 nm by forming a colored complex with diphenylcarbazide (Yalçin and Apak 2004). The detection limit for Cr(VI) was 40 μg/L.

### Zeta-potential measurements

The surface charge of the composite species was measured by estimating the zeta-potential in aqueous solution using light scattering measurements (ELS-8000, Photal, Otsuka Electronics, Japan). The nanocomposite samples was prepared in 1 mM NaCl and ultrasonicated prior to use. To find point of zero charge ($pH_{PZC}$) of the particle, 0.1 M HCl and 0.1 M NaOH were used to adjust the pH.

## Result and discussion

### Characterization of nanocomposites

The XRD analysis of nanocomposites synthesized using different acetone concentrations (0A to 50A) have already been published elsewhere (Lee et al. 2008). For sample 0A, the XRD pattern showed a single peak at 44° indicating the presence of $Fe^0$ as the single phase. However, with increasing acetone concentration, the intensity of the $Fe^0$ peak decreased for samples 5A–50A. Simultaneously, XRD peaks corresponding to magnetite ($Fe_3O_4$) and lepidocrocite ($\gamma$-FeOOH) appeared with increasing acetone concentration. The decrease in the $Fe^0$ peak intensity indicates that the $Fe^{3+}$ reduction process by borohydride is inhibited when the acetone concentration is increased. The overall reaction for nZVI synthesis by borohydride reduction of $Fe^{3+}$ species involves stoichiometric reduction of iron and oxidation of boron with partial oxidation of hydride to hydrogen (Glavee et al. 1995; Wang and Zhang 1997). In protic solvents (like water), however, borohydride can also reduce aldehydes and ketones (Kayser et al. 1982). In this reaction, hydride transfer to the carbonyl moiety results in the formation of tetraalkoxyborates ($R_2(CHO)_4B^-$), which subsequently hydrolyze to the corresponding alcohol. Therefore, synthesis of nZVI with borohydride in a mixture of water and carbonyl-containing organic solvent (like acetone) hinders the $Fe^{3+}$ reduction due to (i) competition between $Fe^{3+}$ and acetone for borohydride ions, resulting in decreased yield of $Fe^0$, and (ii) the formation of intermediate ($R_2(CHO)_4B^-$), which hinders the nucleation of iron particles. The XRD pattern also exhibited a new peak at 11°, which was attributed to an iron oxide precursor (Wang and Li 2003; Pike et al. 2007). The increase in the intensity of this XRD peak with acetone concentration $\geq 25$ % is indicative of phase transformation of iron metal into iron oxide.

By varying the concentration of acetone from 0 to 50 % (v/v), the dispersibility and settling behavior of the nanoparticles also varied considerably (Fig. 1). After 1 h, a sharp difference in settling behavior and color was observed between samples 0A and 10A compared to 25A and 50A. When the concentration of acetone is less than 25 %, the dispersibility and stability of the particles is not enhanced compared to nZVI alone. However, when the concentration is

increased to 25 and 50 %, the particles remain stable and well-dispersed. TEM images (Fig. 2) also indicate that the acetone concentration has a profound effect on the nanocomposite morphology. Samples 0A–10A consist of mainly spherical bead-like particles aggregated into chains of individual units (panel a–c). However, with increasing acetone concentration, the primary particles became less abundant and are associated with increasing quantities of acicular particles (panel d and e). At acetone concentration $\geq 25$ %, the acicular phase is the dominant species, which explains the sharp transition in sedimentation rate observed in Fig. 1. The primary spherical particles are intermittently scattered within the acicular matrix.

The effect of acetone concentration on the chemical composition of the synthesized nano-iron composites was further characterized by measuring the saturation magnetization ($B_s$), $Fe^0$ (%) content ($\chi^{Fe(0)}$) and specific surface area ($a_s$) (Table 1). The $Fe^0$ content decreased from 55 to 23 % with increasing acetone concentration from 0 to 50 %. Based on the magnetization data, 0A (92.1 emu/g) displayed a typical ferromagnetic behavior, whereas, the other nanocomposites (51.9–23.3 emu/g) exhibited magnetic properties intermediate between those of magnetite (66.7 emu/g) and hematite (2.67 emu/g) (Phenrat et al. 2007). The rapid decrease in magnetization with increasing acetone concentration resulted from the inhibition of $Fe^{3+}$ reduction to metallic Fe, which in turn, reduced the total magnetic property of the iron particles. The metallic iron content $\chi^{Fe(0)}$ and saturation magnetization $B_s$ can be correlated to the acetone concentration by Eqs. (1) and (2), respectively.

$$\chi^{Fe(0)}(\%) = 52.9 - (0.55 \times [Acetone]) \tag{1}$$

$$B_s(emu/g) = 4.7 + \left(87.5 \times [Acetone]^{-0.39 \pm 0.02}\right) \tag{2}$$

Thus, all characterization data indicate the formation of iron/iron oxide mixed phase nanocomposites when $Fe^{3+}$ reduction by borohydride is carried out in the presence of increasing concentrations of acetone as co-solvent. To compare the effect of solvent on the stability, ethanol and methanol were used as co-solvents instead of acetone. Using 50 % (v/v) co-solvent concentration, nanocomposites using ethanol
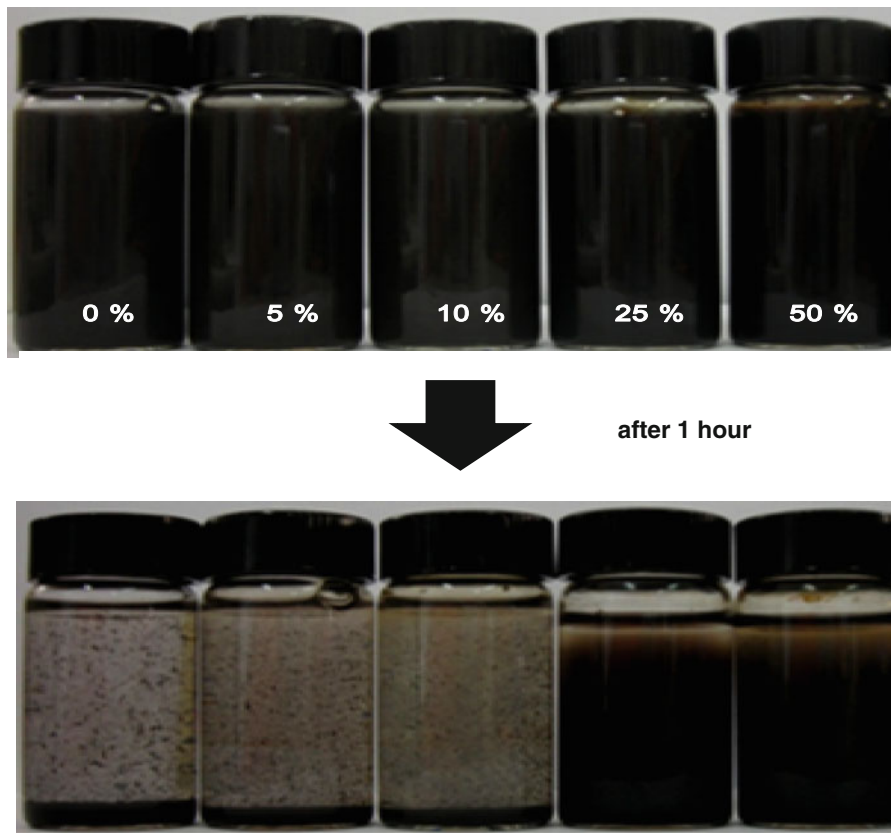
**Fig. 1** Qualitative sedimentation results of synthesized iron–iron oxide nanocomposites

and methanol were synthesized. The sedimentation rates of all nanocomposites (Fig. 3b) indicated that the acetone-based nanocomposites were more dispersed and stable over a long period of time compared to the ethanol and methanol nanocomposites.

### Chromate removal by iron/iron oxide nanocomposites

Using chromate as a model contaminant, we measured the adsorption rate and capacity of these nanocomposites for potential contaminant sequestration. The kinetics of chromate removal from aqueous solution, shown in Fig. 4a and Table 3, can be explained in terms of a pseudo-first-order model. The corresponding rate constants ($k_{obs}$) are summarized in Table 2. Assuming that the effect of nanocomposites concentration on chromate removal is also of first-order

(Alowitz and Scherer 2002), the specific rate constant is defined by Eq. (3)

$$d[Cr(VI)]/dt = -k_m[Cr(VI)] \, [\text{total iron}], \qquad (3)$$

where [total iron] is typically expressed in mg/L. Using this relation, the mass-normalized second-order rate constants ($k_m$) and surface area-normalized rate constants ($k_s$) are listed in Table 2. The rate of Cr(VI) removal was highest for nanocomposites prepared from 50 % acetone concentration (50A), with almost a half of orders of magnitude greater than that for 0A.

Figure 4b shows the adsorption isotherm of Cr(VI) removal for the synthesized nanocomposites. The Langmuir adsorption isotherm model was employed for calculating the chromate removal capacity of the particles. This model was used to show the relationship between the amount of heavy metal absorbed at equilibrium ($q_e$, mg/g) and the equilibrium solute concentration ($C_e$, mg/L) as given in Eq. (4)
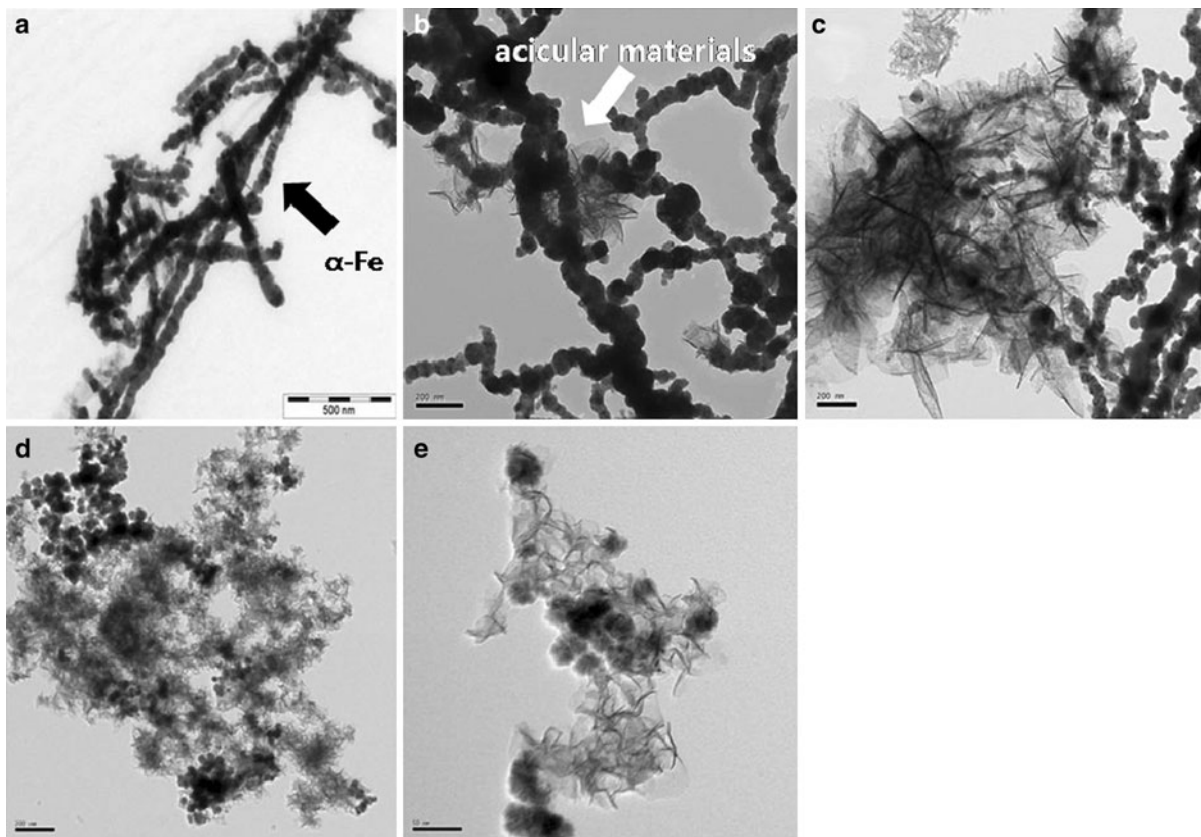
**Fig. 2** TEM image illustrations showing the acicular flower-like arrangement of the synthesized nanocomposites: **a** 0A ($\times 25{,}000$), **b** 10A ($\times 25{,}000$), **c** 25A ($\times 25{,}000$), **d** 50A ($\times 25{,}000$), and **e** 50A ($\times 100{,}000$)

**Table 1** Physico-chemical characterization of iron–iron oxide nanocomposites

| Samples | $B_s$ (emu/g)[a] | $\chi^{Fe(0)}$ (%)[b] | $a_s$ (m²/g)[c] | Carbon (%)[d] |
|---|---|---|---|---|
| 0A | 92.1 | 55 | $33.2 \pm 1.2$ | <1.0 |
| 5A | 51.9 | 50 | $33.5 \pm 1.6$ | <1.0 |
| 10A | 39.5 | 47 | $33.7 \pm 1.8$ | 2.5 |
| 25A | 28.7 | 38 | $125.0 \pm 2.3$ | 21.4 |
| 50A | 23.3 | 23 | $141.1 \pm 9.1$ | 22.5 |

[a] Saturation magnetization, [b] analysis method was followed using Liu et al. (2005), [c] mean and average deviation from duplicate analysis, [d] by TOC analyzer

$$q_e = \frac{q_{max} b C_e}{1 + b C_e}, \qquad (4)$$

where $q_{max}$ (mg/g) is the maximum adsorption capacity corresponding to the complete adsorption on the particle surface and $b$ is the equilibrium constant

(mg/L) used to evaluate the removal ability for heavy metals (Chiron et al. 2003; Zhong et al. 2006). The initial concentration of chromate was fixed at 20 mg/L and iron dosage varied from 1.5 to 1,500 mg/L. The removal of Cr(VI) fit well with the Langmuir isotherm as shown in Fig. 4b and the maximum adsorption capacity ($q_{max}$) was elucidated. The minimum and maximum values of $q_{max}$ were found to be 20.1 mg/g (for 0A) and 34.1 mg/g (for 50A), respectively.

To critically understand the adsorption behavior of these nanocomposites, the rate of change of total adsorption capacity ($q$) was studied for all nanocomposites (Fig. 4c). It is clearly evident that nanocomposite synthesized at 50 % acetone concentration exhibited the highest adsorption rate among all nanocomposites. This is in agreement with the Cr(VI) removal kinetics, as shown in Fig. 4a. Thus, at an optimum co-solvent concentration, highly dispersed particles with large surface area (see Table 1) facilitates rapid and enhanced Cr(VI) adsorption on the
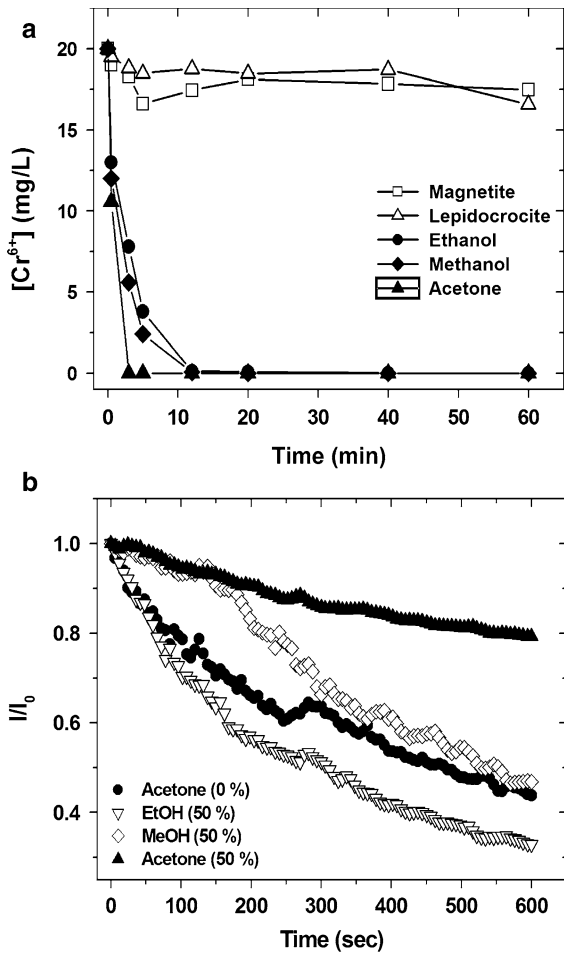
**Fig. 3** **a** Effect of different co-solvents (used to synthesize the nanocomposite) and iron oxides on Cr(VI) uptake and adsorption and **b** rate of sedimentation of native nZVI and nanocomposites synthesized by using various co-solvents

catalyst surface. This is expected since adsorption capacity is critically dependent on the available surface area, and nanocomposite 50A showed the largest surface area compared to other nanocomposites (Table 1). Also, the $N_2$ adsorption and desorption isotherms for 50A (Fig. 5a) showed prominent hysteresis, indicating the porous nature of the composite. The pore size distribution (Fig. 5b) exhibited a maximum at 5 nm, which further confirmed that the sample was mesoporous in nature. Thus, the high surface area and porous nature of the nanocomposite 50 A is responsible for the enhanced removal of Cr(VI) from aqueous solution.

Figure 6 shows the zeta-potential of the nanocomposites at various pH values. The $pH_{PZC}$ for the iron–
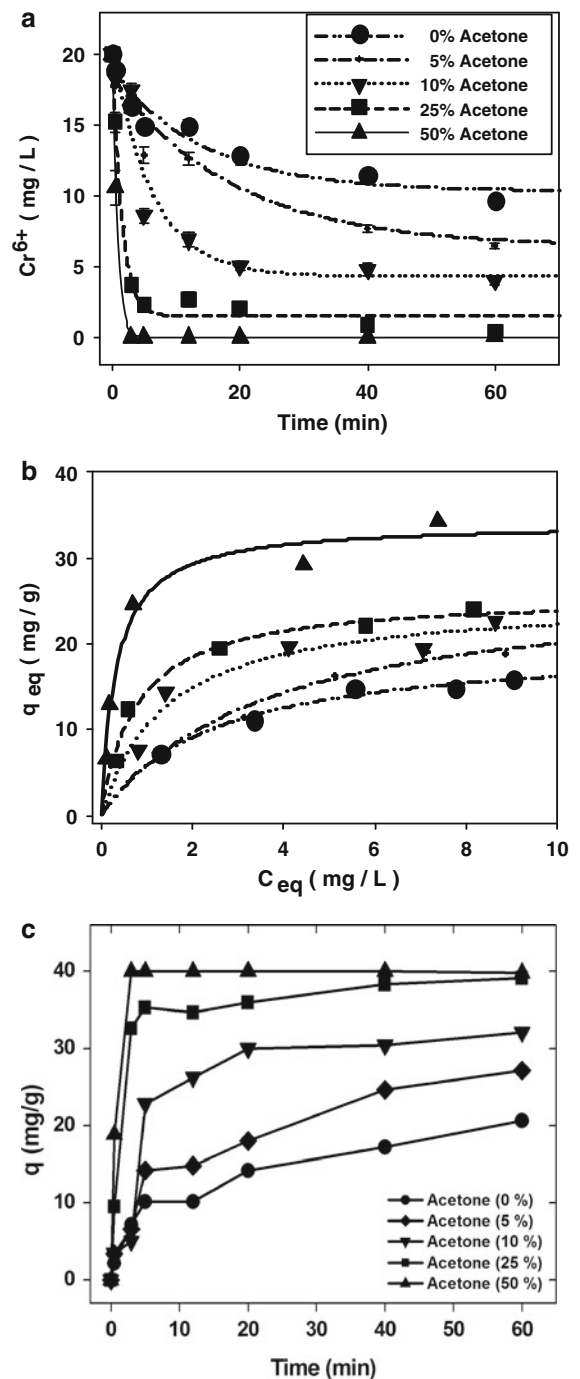


**Fig. 4** **a** Kinetics of Cr(VI) removal from aqueous solutions. The *curves* were fitted by pseudo-first-order model (Eq. 3). **b** Adsorption equilibrium isotherms of the synthesized nanocomposites. The curves were fitted according to the Langmuir model. In both cases, [Cr(VI)] = 20 mg/L and $pH_i$ 6.0. In **b**, contact time = 6 h and **c** adsorption kinetics by the synthesized nanocomposites [Cr(VI)] = 20 mg/L and $pH_i$ 6.0]

**Table 2** Kinetics of Cr(VI) adsorption by the synthesized iron–iron oxide nanocomposites

| Samples | $k_{obs} \times 10^4$ $(s^{-1})$[a] | $k_m \times 10^4$ $(L\text{-}g^{-1}\ s^{-1})$[b] | $k_{sa} \times 10^6$ $(L\text{-}m^{-2}\ s^{-1})$[c] | $q_{max}$ $(mg/g)$[d] |
|---|---|---|---|---|
| 0A | $1.4 \pm 0.1$ | $2.5 \pm 0.1$ | $7.5 \pm 0.4$ | 20.1 |
| 5A | $2.7 \pm 0.1$ | $4.8 \pm 0.1$ | $14.2 \pm 0.7$ | 27.5 |
| 10A | $4.2 \pm 0.2$ | $7.6 \pm 0.4$ | $23.9 \pm 1.8$ | 25.3 |
| 25A | $77 \pm 5.5$ | $101 \pm 7.3$ | $65.3 \pm 4.9$ | 25.6 |
| 50A | $715 \pm 4.1$ | $937 \pm 13.6$ | $664 \pm 24$ | 34.1 |

[a] Uncertainties are 95 % confidence intervals for pseudo-first-order fit of product data, [b,c] 95 % confidence limits calculated from the uncertainties in $k_{obs}$, calculated by propagation of error, [d] from fitting Langmuir isotherms (Eq. 4)

iron oxide nanocomposite was ~8.0 and the zeta-potential ranged from 26.51 to −22.49 mV. In the Cr(VI) removal experiments, the initial pH was 6. At this pH, the nanocomposites carry a positive charge (according to Fig. 6) and $HCrO_4^-$ is the dominant Cr(VI) species (Bokare and Choi 2010). Thus, the positive charge on the nanoparticles results in electrostatic attraction of the negatively charged Cr(VI) species, resulting in efficient adsorption on the nanoparticles surface.

Chromate reduction on nanocomposite surface

XPS analysis was carried out to indentify the chromium species on the surface of 50A after adsorption. Figure 7 shows the Cr 2p XPS peaks after 10 min and 6 h adsorption studies. It is known that the binding energy of the $Cr(2p_{3/2})$ line for Cr(VI) salts like $K_2CrO_4$ and $Na_2CrO_4$ is found at 580 eV, while the peaks at binding energy 576.0–577.6 eV correspond to Cr(III) oxyhydroxides such as CrOOH and $Cr(OH)_3$

(Pratt et al. 1997; Loyaux-Lawniczak et al. 2000; Legrand et al. 2004). It is also reported that the magnitude of spin–orbit splitting between the two peaks can distinguish Cr(III) from Cr(VI) (Legrand et al. 2004; Li et al. 2008). The 2p spin orbit splitting of 9.7–9.9 eV is characteristic for Cr(III) species, whereas, a value of 8.7–9.4 eV belongs to Cr(VI) species. In the case of 50A (Fig. 7), the binding energy of the $2p_{3/2}$ and $2p_{1/2}$ peaks are 577.6 and 587.4 eV, respectively, and the spin–orbit splitting is 9.8 eV. These values are consistent with the characteristics of Cr(III) species (Pratt et al. 1997). Thus, the presence of Cr(III) on the surface indicates that Cr(VI) removal from solution proceeded by rapid adsorption (within 10 min) and subsequent reduction to Cr(III) by the $Fe^0$ species present in the nanocomposite.

The reduction of Cr(VI) by nZVI is an essentially heterogeneous reaction due to its strong dependence on the iron surface area and observed inhibition in the absence of water (Gillham and Ohannesin 1994). Zachara et al. (1987) have suggested that adsorption is the first step in the reduction of Cr(VI) by nZVI or iron oxide (i.e., magnetite) and the reduction reaction cannot be catalyzed by $Fe^{2+}$ or by $H_2$ formed in the $Fe^0$-water corrosion reaction (Matheson and Tratnyek 1994). Since, a surface-catalyzed direct electron transfer is the predominant pathway for reduction reactions on the iron particles, rapid adsorptive removal of the pollutant from aqueous solution always precedes electron transfer for reduction. More importantly, the initial high rate of uptake and removal is followed by decrease in reduction rate regardless of the contaminant species or concentration. This indicates that the removal mechanism involves physisorption on the iron surface and not chemisorption. Hence, we can safely rule out Cr(VI) reduction via non-

**Table 3** Quantitative analysis of $Cr^{total}$ in aqueous solution

| Time (min) | $Cr^{total}$ (µmol) | | | | |
|---|---|---|---|---|---|
| | 0A | 5A | 10A | 25A | 50A |
| 0 | 384.6 | 384.6 | 384.6 | 384.6 | 384.6 |
| 0.5 | $363.4 \pm 1.4$ | $352.3 \pm 0$ | $351.7 \pm 4.8$ | $292.9 \pm 13.5$ | $203.3 \pm 3.1$ |
| 3 | $315.4 \pm 3.8$ | $321.1 \pm 3.1$ | $336.5 \pm 4.1$ | $70.9 \pm 7.0$ | 0 |
| 5 | $286.5 \pm 7.1$ | $248.1 \pm 11.7$ | $165.5 \pm 9.2$ | $44.7 \pm 5.2$ | 0 |
| 12 | $286.5 \pm 5.6$ | $242.3 \pm 7.6$ | $132.6 \pm 9.2$ | $51.2 \pm 9.2$ | 0 |
| 20 | $241.8 \pm 4.6$ | $240.4 \pm 7.1$ | $96.4 \pm 6.2$ | $38.4 \pm 5.0$ | 0 |
| 40 | $219.2 \pm 4.4$ | $147.9 \pm 5.2$ | $92.0 \pm 4.3$ | $16.3 \pm 1.9$ | 0 |
| 60 | $186.5 \pm 3.7$ | $123.8 \pm 3.1$ | $76.3 \pm 5.0$ | $8.3 \pm 1.9$ | 0 |

$Cr^{total}$ was measured by ICP
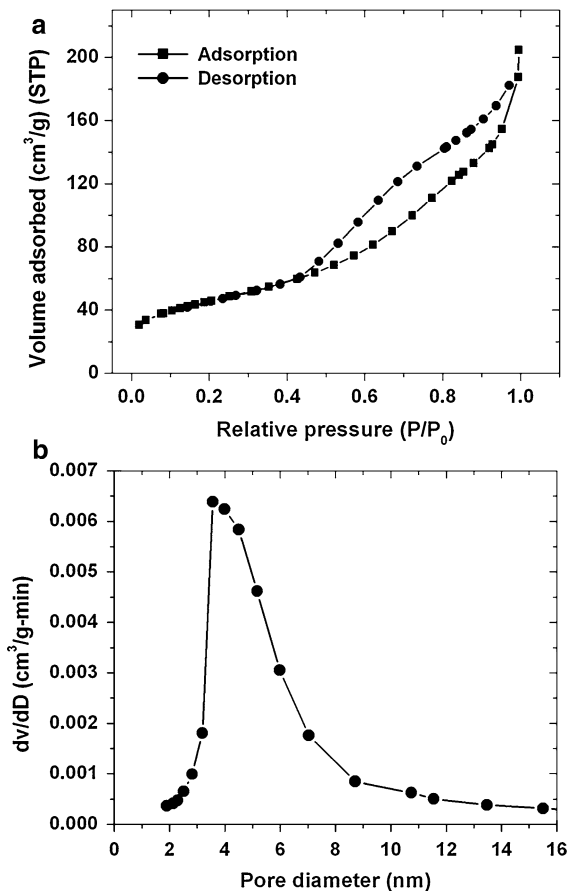
Fig. 5 **a** $N_2$ adsorption–desorption isotherms. **b** Pore size distribution of the iron–iron oxide nanocomposite 50A
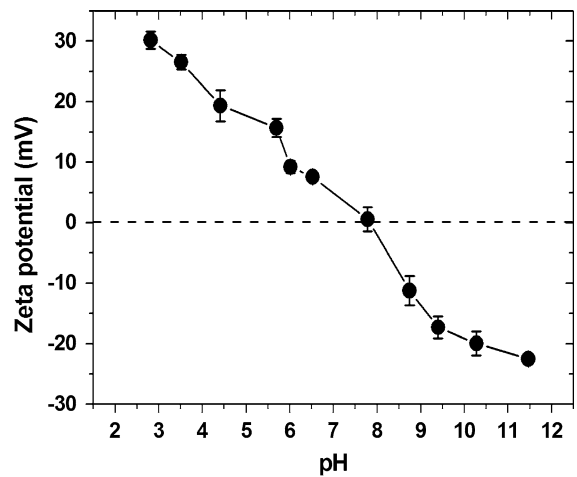


Fig. 6 Electrophoretic mobility (EPM) of the 50A nanocomposite as a function of pH. Each data point represents the mean of at least a total of five measurements of at least two different samples at each pH, and the *error bars* represent standard deviations. Measurements were conducted at 25 °C
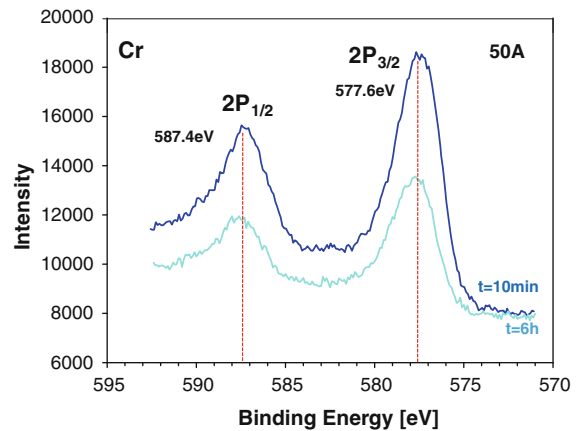


Fig. 7 Core level Cr 2p XPS spectra of 50A nanocomposite at $t = 10$ min and 6 h

adsorptive reduction pathway and the formation of $Cr^{III}$-hydroxide can only occur on the nanocomposite surface.

Interestingly, the chromate removal efficiency by adsorption–reduction shows a strong correlation with the concentration of acetone added during nanocomposite synthesis. The removal rate ($k_{sa}$) and adsorptive capacity ($q_{max}$) for Cr(VI) was maximum for nanocomposite 50A. It is expected that the Cr(VI) removal rate must be dependent on the $Fe^0$ content in the nanocomposite ($\chi^{Fe(0)}$) due to its involvement in direct electron transfer to Cr(VI) (Ponder et al. 2000). However, the Cr(VI) removal data showed that the nanocomposite with the lowest $\chi^{Fe(0)}$ value (50A) demonstrated the highest removal rate, whereas, particles with the highest $\chi^{Fe(0)}$ value (0A) showed the lowest removal efficiency (Tables 1, 2). This shows that the increase in the active surface area on the

nanocomposite is more critical for enhancing the adsorption capacity for Cr(VI), making it easy for direct electron transfer from $Fe^0$ to Cr(VI) on the surface. Also, the post-reaction analysis of the synthetic nanocomposites after treatment revealed that the acicular material adsorbed more chromium than the spherical iron particles. TEM–EDX analysis of various regions on the nanocomposites revealed that the atomic ratio of Cr to Fe at the acicular matrix was about 8 times higher than the corresponding ratio on the spherical particles (Fig. 8A, B). In nanocomposite 50A, the higher surface area due to the
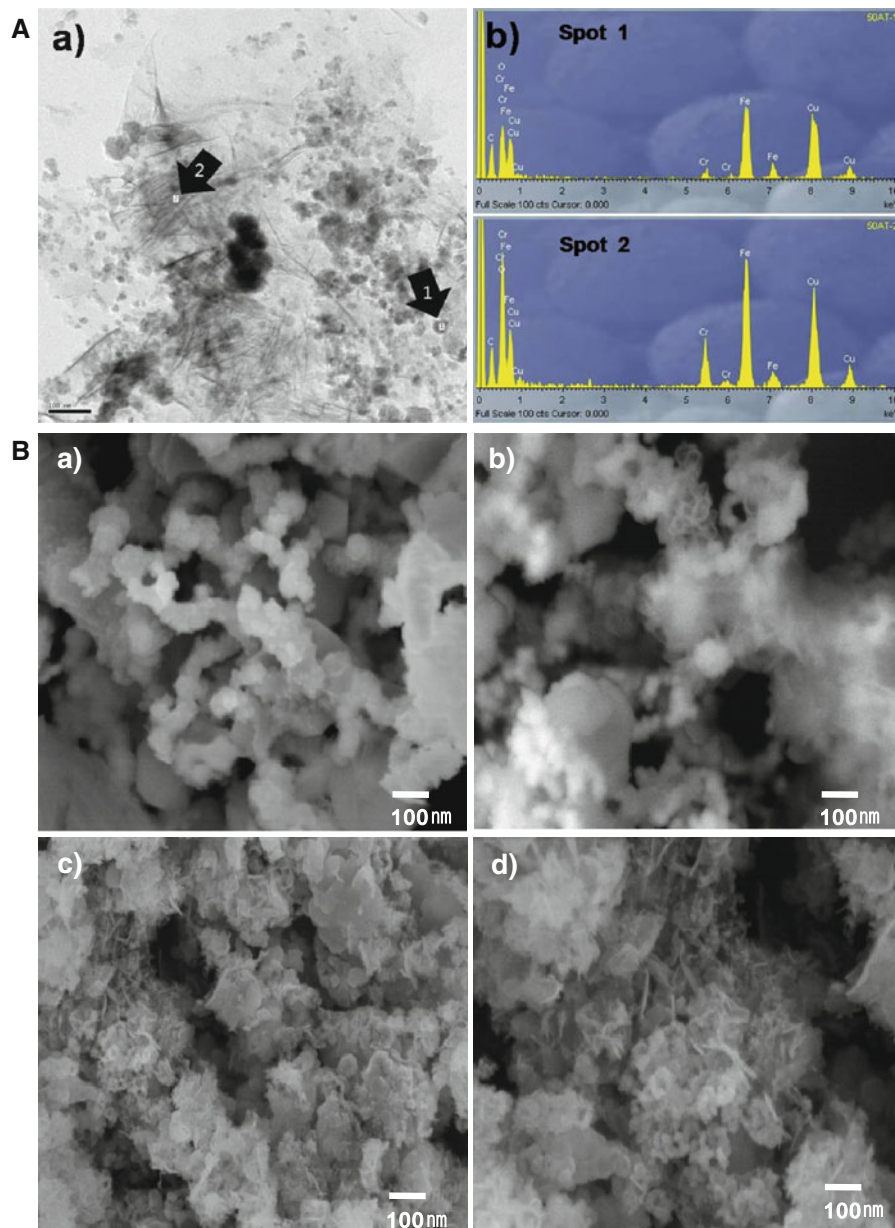
**Fig. 8 A** EDX analysis and elemental mapping of 50A nanocomposite (spots 1 and 2 denote the atomic ratio of Cr/Fe on the surface of the acicular matrix). **B** SEM image illustrations showing the acicular matrix of the synthesized nanocomposites: (*a*) 0A (×25,000), (*b*) 10A (×25,000), (*c*) 25A (×25,000), (*d*) 50A (×25,000), (*e*) 50A (×100,000)

formation of mesoporous oxides with acicular-like morphology played a dominant role in the enhanced uptake of Cr(VI) and its subsequent reduction to Cr(III). Figure 3a shows the Cr(VI) removal activity of ethanol- and methanol-based nanocomposites. Although, complete removal of Cr(VI) from aqueous solution was achieved using both nanocomposites, the

rate of Cr(VI) removal was lower compared to the acetone-based nanocomposite. Control experiments using lepidocrocite [$\gamma$-FeOOH)] and magnetite [$Fe_3O_4$] also showed negligible activity towards Cr(VI) adsorption and removal (Fig. 3a).

Thus, 50 % acetone concentration (v/v) is the optimum value for synthesis of porous iron oxide

nanoparticles with ZVI core for rapid and effective Cr(VI) removal by sequential adsorption–reduction. In contrast to the traditional methods for the preparation of porous metal oxide nanomaterials (iron oxide and manganese oxides) like hydrothermal treatment or thermal decomposition (Shen et al. 1993; Zhong et al. 2006), our synthesis procedure involves a simple addition of acetone as the carbonyl moiety responsible for mesoporosity. By adjusting the acetone concentration, the desired porosity and acicular flower-like arrangement can be easily achieved at ambient conditions, without the need for elevated temperatures and/or strict synthesis protocols. Such nanocomposites have high potential to be used as adsorbent-cum-reductant catalysts for metal decontamination.

## Conclusion

A facile procedure for the preparation of stable and dispersed suspension of mesoporous nano-iron–iron oxide composites is illustrated. The addition of optimum concentration of acetone as co-solvent hindered the nucleation of $Fe^0$ particles, and consequently changed the composition of synthetic particles. As a result, porous nano-iron composites with high surface area were obtained through a one-pot reaction under ambient conditions. The synthetic nano-iron composites showed enhanced rate constants for Cr(VI) (used as a model pollutant) removal at near-neutral pH by sequential adsorption–reduction to Cr(III) on the catalyst surface. No harsh conditions (acidic pH or high temperatures) were used in this study, which make these nanocomposites ideal catalysts for metal detoxification in aqueous solutions.

## References

Alowitz MJ, Scherer MM (2002) Kinetics of nitrate, nitrite, and Cr(VI) reduction by iron metal. Environ Sci Technol 36:299–306

Bokare AD, Choi W (2010) Chromate-induced activation of hydrogen peroxide for oxidative degradation of aqueous organic pollutants. Environ Sci Technol 44:7232–7237

Bond DL, Fendorf S (2003) Kinetics and structural constraints of chromate reduction by green rusts. Environ Sci Technol 37:2750–2757

Bonder MJ, Zhang Y, Kiick KL, Papaefthymiou V, Hadjipanayis GC (2007) Controlling synthesis of Fe nanoparticles with polyethylene glycol. J Magn Magn Mater 311:658–664

Carpenter EE (2001) Iron nanoparticles as potential magnetic carriers. J Magn Magn Mater 225:17–20

Chang LY (2005) Chromate reduction in wastewater at different pH levels using thin iron wires—a laboratory study. Environ Prog 24:305–316

Chen SS, Cheng CY, Li CW, Chai PH, Chang YM (2007) Reduction of chromate from electroplating wastewater from pH 1 to 2 using fluidized zero valent iron process. J Hazard Mater 142:362–367

Chiron N, Guilet R, Deydier E (2003) Adsorption of Cu(II) and Pb(II) onto a grafted silica: isotherms and kinetic models. Water Res 37:3079–3086

Eisazadeh H (2007) Removal of chromium from waste water using polyaniline. J Appl Polym Sci 104:1964–1967

Fendorf SE, Li G (1996) Kinetics of chromate reduction by ferrous iron. Environ Sci Technol 30:1614–1617

Flury B, Frommer J, Eggenberger U, Mäder U, Nachtegaal M, Kretzschmar R (2009) Assessment of long-term performance and chromate reduction mechanisms in a field scale permeable reactive barrier. Environ Sci Technol 43:6786–6792

Gillham RW, Ohannesin SF (1994) Enhanced degradation of halogenated aliphatics by zero valent iron. Ground Water 32:958–967

Glavee GN, Klabunde KJ, Sorensen CM, Hadjipanayis GC (1995) Chemistry of borohydride reduction of iron(II) and iron(III) ions in aqueous and nonaqueous media. Formation of nanoscale Fe, FeB, and $Fe_2B$ powders. Inorg Chem 34:28–35

Gupta S, Babu BV (2009) Utilization of waste product (tamarind seeds) for the removal of Cr(VI) from aqueous solutions: equilibrium, kinetics, and regeneration studies. J Environ Manage 90:3013–3022

Jeen SW, Blowes DW, Gillham RW (2008) Performance evaluation of granular iron for removing hexavalent chromium under different geochemical conditions. J Contam Hydrol 95:76–91

Jiang Z, Lv L, Zhang W, Du Q, Pan B, Yang L, Zhang Q (2011) Nitrate reduction using nanosized zero-valent iron supported by polystyrene resins: role of surface functional groups. Water Res 45:2191–2198

Kanel SR, Choi H (2007) Transport characteristics of surface-modified nanoscale zero-valent iron in porous media. Water Sci Technol 55:157–162

Kayser MM, Eliev S, Eisenstein O (1982) Reduction of ketones by sodium borohydride in the absence of protic solvents. Inter versus intramolecular mechanism. Tetrahedron Lett 24:1015–1018

Kendelewicz T, Liu P, Doyle CS, Brown GE Jr (2000) Spectroscopic study of the reaction of aqueous Cr(VI) with Fe3O4(111) surfaces. Surf Sci 469:144–163

Kim JH, Tratnyek PG, Chang YS (2008) Rapid dechlorination of polychlorinated dibenzo-p-dioxins by bimetallic and nanosized zerovalent iron. Environ Sci Technol 42:4106–4112

Kowalski Z (1994) Treatment of chromic tannery wastes. J Hazard Mater 37:137–141

Lee JM, Kim JH, Lee JW, Kim JH, Lee HS, Chang YS, Nurmi JT, Tratnyek PG (2008) Synthesis of Fe-nano particles obtained by borohydride reduction with solvent. In: International conference on remediation of chlorinated and recalcitrant compounds

Legrand L, El Figuigui A, Mercier F, Chausse A (2004) Reduction of aqueous chromate by Fe(II)/Fe(III) carbonate green rust: kinetic and mechanistic studies. Environ Sci Technol 38:4587–4595

Li XQ, Cao J, Zhang WX (2008) Stoichiometry of Cr(VI) immobilization using nanoscale zero valent iron (nZVI): a study with high-resolution X-ray photoelectron spectroscopy (HR-XPS). Ind Eng Chem Res 47:2131–2139

Liu Y, Majetich SA, Tilton RD, Sholl DS, Lowry GV (2005) TCE dechlorination rates, pathways, and efficiency of nanoscale iron particles with different properties. Environ Sci Technol 39:1338–1345

Liu Y, Phenrat T, Lowry GV (2007) Effect of TCE concentration and dissolved groundwater solutes on NZVI-promoted TCE dechlorination and $H_2$ evolution. Environ Sci Technol 41:7881–7887

Loyaux-Lawniczak S, Refait P, Ehrhardt JJ, Lecomte P, Génin JMR (2000) Trapping of Cr by formation of ferrihydrite during the reduction of chromate ions by Fe(II)–Fe(III) hydroxysalt green rusts. Environ Sci Technol 34:438–443

Ludwig RD, Su C, Lee TR, Wilkin RT, Acree SD, Ross RR, Keeley A (2007) In situ chemical reduction of Cr(VI) in groundwater using a combination of ferrous sulfate and sodium dithionite: a field investigation. Environ Sci Technol 41:5299–5305

Lv X, Xu J, Jiang G, Xu X (2011) Removal of chromium(VI) from wastewater by nanoscale zero-valent iron particles supported on multiwalled carbon nanotubes. Chemosphere 85:1204–1209

Margeat O, Dumestre F, Amiens C, Chaudret B, Lecante P, Respaud M (2005) Synthesis of iron nanoparticles: size effects, shape control and organisation. Prog Solid State Chem 33:71–79

Matheson LJ, Tratnyek PG (1994) Reductive dehalogenation of chlorinated methanes by iron metal. Environ Sci Technol 28:2045–2053

Park SJ, Jang YS (2002) Pore structure and surface properties of chemically modified activated carbons for adsorption mechanism and rate of Cr(VI). J Colloid Interface Sci 249:458–463

Periasamy M, Thirumalaikumar M (2000) Methods of enhancement of reactivity and selectivity of sodium borohydride for applications in organic synthesis. J Organomet Chem 609:137–151

Pettine M, D'Ottone L, Campanella L, Millero FJ, Passino R (1998) The reduction of chromium (VI) by iron (II) in aqueous solutions. Geochim Cosmochim Acta 62:1509–1519

Phenrat T, Saleh N, Sirk K, Tilton RD, Lowry GV (2007) Aggregation and sedimentation of aqueous nanoscale zerovalent iron dispersions. Environ Sci Technol 41:284–290

Pike J, Hanson J, Zhang L, Chan SW (2007) Synthesis and redox behavior of nanocrystalline Hausmannite ($Mn_3O_4$). Chem Mater 19:5609–5616

Pillay K, Cukrowska EM, Coville NJ (2009) Multi-walled carbon nanotubes as adsorbents for the removal of parts per billion levels of hexavalent chromium from aqueous solution. J Hazard Mater 166:1067–1075

Ponder SM, Darab JG, Mallouk TE (2000) Remediation of Cr(VI) and Pb(II) aqueous solutions using supported, nanoscale zero-valent iron. Environ Sci Technol 34:2564–2569

Pratt AR, Blowes DW, Ptacek CJ (1997) Products of chromate reduction on proposed subsurface remediation material. Environ Sci Technol 31:2492–2498

Saleh N, Phenrat T, Sirk K, Dufour B, Ok J, Sarbu T, Matyjaszewski K, Tilton RD, Lowry GV (2005) Adsorbed triblock copolymers deliver reactive iron nanoparticles to the oil/water interface. Nano Lett 5:2489–2494

Saleh N, Kim HJ, Phenrat T, Matyjaszewski K, Tilton RD, Lowry GV (2008) Ionic strength and composition affect the mobility of surface-modified fe0 < nanoparticles in water-saturated sand columns. Environ Sci Technol 42:3349–3355

Schrick B, Hydutsky BW, Blough JL, Mallouk TE (2004) Delivery vehicles for zerovalent metal nanoparticles in soil and groundwater. Chem Mater 16:2187–2193

Sedlak DL, Chan PG (1997) Reduction of hexavalent chromium by ferrous iron. Geochim Cosmochim Acta 61:2185–2192

Shen YF, Zerger RP, DeGuzman RN, Suib SL, McCurdy L, Potter DI, O'Young CL (1993) Manganese oxide octahedral molecular sieves: preparation, characterization, and applications. Science 260:511–515

Shi LN, Zhang X, Chen ZL (2011) Removal of chromium(VI) from wastewater using bentonite-supported nanoscale zero-valent iron. Water Res 45:886–892

Taghavy A, Costanza J, Pennell KD, Abriola LM (2010) Effectiveness of nanoscale zero-valent iron for treatment of a PCE-DNAPL source zone. J Contam Hydrol 118:128–142

Wang X, Li Y (2003) Synthesis and formation mechanism of manganese dioxide nanowires/nanorods. Chem Eur J 9:300–306

Wang CB, Zhang WX (1997) Synthesizing nanoscale iron particles for rapid and complete dechlorination of TCE and PCBs. Environ Sci Technol 31:2154–2156

Wang W, Jin Zh, Tl Li, Zhang H, Gao S (2006) Preparation of spherical iron nanoclusters in ethanol–water solution for nitrate removal. Chemosphere 65:1396–1404

Wang Q, Snyder S, Kim J, Choi H (2009) Aqueous ethanol modified nanoscale zerovalent iron in Bromate reduction: synthesis, characterization, and reactivity. Environ Sci Technol 43:3292–3299

Xu Y, Zhao D (2007) Reductive immobilization of chromate in water and soil using stabilized iron nanoparticles. Water Res 41:2101–2108

Yalçin S, Apak R (2004) Chromium(III, VI) speciation analysis with preconcentration on a maleic acid-functionalized XAD sorbent. Anal Chim Acta 505:25–35

Zachara JM, Girvin DC, Schmidt RL, Thomas Resch C (1987) Chromate adsorption on amorphous iron oxyhydroxide in the presence of major groundwater ions. Environ Sci Technol 21:589–594

Zhong LS, Hu JS, Liang HP, Cao AM, Song WG, Wan LJ (2006) Self-assembled 3D flowerlike iron oxide nanostructures and their application in water treatment. Adv Mater 18:2426–2431

Zhu J, Wei S, Gu H, Rapole SB, Wang Q, Luo Z, Haldolaarachchige N, Young DP, Guo Z (2011) One-pot synthesis of magnetic graphene nanocomposites decorated with core@double-shell nanoparticles for fast chromium removal. Environ Sci Technol 46:977–985